Cycle dynamics and synchronization in a coupled network of peripheral circadian clocks

Odile Burckard[1], Michèle Teboul[2], Franck Delaunay[2], and Madalena Chaves[1,*]

[1]Université Côte d'Azur, Inria, INRAE, CNRS, Sorbonne Université, Biocore team, Sophia Antipolis, France
[2]Université Côte d'Azur, CNRS, Inserm, iBV, France
[*]Corresponding author. Email: madalena.chaves@inria.fr

Abstract

The intercellular interactions between peripheral circadian clocks, located in tissues and organs other than the suprachiasmatic nuclei of the hypothalamus, are still very poorly understood. We propose a theoretical and computational study of the coupling between two or more clocks, using a calibrated, reduced model of the circadian clock to describe some synchronization properties between peripheral cellular clocks. Based on a piecewise linearization of the dynamics of the mutual CLOCK:BMAL1 / PER:CRY inactivation term, we suggest a segmentation of the circadian cycle into six stages, to help analyse different types of synchronization between two clocks, including single stage duration, total period, and maximal amplitudes. Finally, our model reproduces some recent experimental results on the effects of different regimes of time-restricted feeding in liver circadian clocks of mice.

1 Introduction

Most organisms have evolved a circadian timing system to synchronize their physiology and behavior with the Earth's light/dark cycle. The core mechanism underlying circadian rhythms is a molecular clock governed by an oscillatory gene network present in virtually all cells and which translates the external time information into optimally phased molecular and cellular rhythms [21]. Environmental or genetic disruption of the circadian clock leads to multiple metabolic alterations in animal models. In humans, misalignment between body time and social time caused for instance by rotating shiftwork or work at night is also a risk factor for cardio-metabolic, inflammatory and malignant diseases [18]. Reciprocally, diseases perturb the circadian coordination thus potentially leading to a vicious cycle. A large body of experimental and clinical evidence suggests that high amplitude and correctly phased oscillations of core clock and clock-controlled genes is a hallmark of health while disrupted or desynchronized rhythms are associated with pathology [17, 23]. Whether and how cells temporally coordinate

together at the scale of the tissue and organ is therefore a question of primary importance to later implement preventive or therapeutic strategies aiming at reinforcing circadian rhythms.

It is now well established that neurons of the central clock located in the suprachiasmatic nuclei (SCN) of the hypothalamus oscillate in synchrony so that a single phase is observed at the tissue level. The coupling mechanism within the SCN requires intercellular communication through gap junctions and neurotransmitters [10]. Intercellular coupling is an important determinant of oscillator amplitude, robustness and entrainment by synchronizers. The SCN encompasses a pacemaker clock that hierarchically controls other peripheral circadian clocks [13]. It is a largely accepted idea that peripheral clocks function mostly as "slave" oscillators that damp in the absence of internal systemic synchronizers such as body temperature and glucocorticoid hormones.

However, this view has been recently challenged by *in vivo* experiments performed in mice performed by Schibler's laboratory [20]. By using a sophisticated technology allowing longitudinal long-term bioluminescence recordings in free living animals, the authors could demonstrate that oscillations of the core clock gene *Rev-erbα* persist in the livers of animals lacking a functional SCN or circadian oscillators in all extra-hepatic organs. Therefore, it appears that phase coherence between hepatocyte clocks can be achieved independently of external Zeitgebers, suggesting that intercellular coupling may occur in the liver. Another recent work [12] by Kramer's laboratory using the human osteosarcoma U2OS cell line reinforces this hypothesis by providing evidence that peripheral cellular oscillators couple *in vitro via* paracrine factors. This study further identified transforming growth factor β (TGFβ) as a candidate signaling molecule contributing to the intercellular coupling between circadian oscillators although this remains to be established *in vivo*.

In this paper, we propose a theoretical and computational study of the coupling between two or more clocks, to investigate the question of intercellular coupling between peripheral circadian oscillators. Our objective is to analyze the dynamical evolution and coordination between the main processes involved in intercellular coupling, to better understand the mechanisms leading to oscillator synchronization. For this study, we will use a reduced mathematical model of the circadian clock previously developed in our group by Almeida et al. [2, 1], which recovers important properties such as the interactions with the cell cycle. This model is calibrated with data from mouse fibroblast cells cultured in regular medium [11], so we can assume that it is a faithful model of an autonomous peripheral clock.

Mathematical models have been developed specifically for the SCN clock [14], for other organs such as the liver [24] or pancreatic beta-cells [25], but more often for "generic" type cells, blending literature data from various sources [19, 8, 2]. Synchronization of neurons in the SCN is studied through a general model in [16] and further detailed in [10], showing the coupling mechanism requires intercellular communication through gap junctions and neurotransmitters.

Synchronization of clocks in other organs or tissues has been studied essentially as a result of SCN control or by entrainment to external cues such as light or food intake [24, 25]. In this study, we suggest a segmentation of the circadian cycle into six stages based on a piecewise linearization of our model [1], to help characterize the effect of coupling on the synchronization mechanism. We find that clock synchronization happens at distinct levels: for instance, clocks with slightly differing periods can synchronize both their amplitudes and periods but maintain distinct duration for each of the six cycle stages. For a cluster of neighbouring cells, our coupling model reproduces some of the recent results on mouse hepatocytes [20], suggesting a relevant role for peripheral clock coupling.

2 Coupling and synchronization of two clock models

The circadian clock model used in this paper was developed in our group [2, 1] and focuses on the transcriptional details of the two main feedback loops present in the circadian clock mechanism [21, 19, 8], both centered on the protein complex CLOCK:BMAL1, next briefly described. In this reduced model, paralogous proteins are not distinguished so that for instance the REV variable accounts for both REV-ERBα and REV-ERBβ. The complex CLOCK:BMAL1 promotes transcription of the genes *Per* and *Cry*, whose corresponding proteins PER and CRY dimerize to form another complex, PER:CRY. Subsequently, upon nuclear translocation, PER:CRY interacts with CLOCK:BMAL1 and the resulting complex is exported from the nucleus, thus blocking CLOCK:BMAL1 transcriptional activity and closing the first negative feedback loop. In parallel, the complex CLOCK:BMAL1 also promotes transcription of the genes *Dbp* and *Rev-erb*α. The protein DBP binds to the D-box clock controlled element located in the *Per* and *Rev-erb*α promoters to activate their transcription. Finally, protein REV-ERBα binds to the R-box in the *Bmal1* promoter, thereby blocking synthesis of the protein BMAL1 and closing the second negative feedback loop.

The reduced form of the model studied in [1] describes the dynamics of the protein complexes CLOCK:BMAL1 (denoted B), DBP (denoted D), REV (denoted R), and PER:CRY (denoted P). The simplified interaction diagram is depicted in Fig. 1 and the ordinary differential equations model from [1] can be written as:

$$
\begin{aligned}
\dot{B} &= V_R h^-(R) - \gamma_B BP, \\
\dot{D} &= V_B B - \gamma_D D, \\
\dot{R} &= V_D D - \gamma_R R, \\
\dot{P} &= V_D D - \gamma_B BP,
\end{aligned}
\tag{1}
$$

where $h^-(R) = \frac{k_R^4}{k_R^4 + R^4}$ is a decreasing function. The model was calibrated with REV-ERBα experimental data from [11] and its concentration units are in percentages of the REV-ERBα data mean value, which was used to normalize the data (see [2]). The set of estimated parameters can be found in Table 2 of [1] and is used throughout this paper (unless stated otherwise):

$$
V_R = 44.4\%.h^{-1}, k_R = 80.1\%, V_B = 0.142\%.h^{-1}, V_D = 19\%.h^{-1}
$$
$$
\gamma_R = 0.241 h^{-1}, \gamma_D = 0.156 h^{-1}, \gamma_B = 2.58 h^{-1},
\tag{2}
$$

with a period of $\tau_1 = 24.5$ hours.

2.1 Coupling between two peripheral clocks

To study the coupling between two or more oscillators, we will include two new observations into our model (1): the variation of the oscillator's period depending on expression level of gene *Cry2* [26] and the role of gene *Per2* in intercellular clock communication [12]. Although the proteins CRY and PER are not specifically represented in system (1), their complex PER:CRY is described by variable P. Therefore, both new observations will be modeled by modifying equation $\dot{P}$ in two different ways, as follows.

To represent circadian period variability among a population of cells, we will follow experimental results showing that *Cry2* knockout or knockdown cells have a longer period than wild type cells [6, 26]. To represent this in our model, we add a factor ε in the equation of PER:CRY, $\dot{P} = \varepsilon V_D D - \gamma_B BP$, where $\varepsilon < 1$ describes a lower availability of protein CRY2
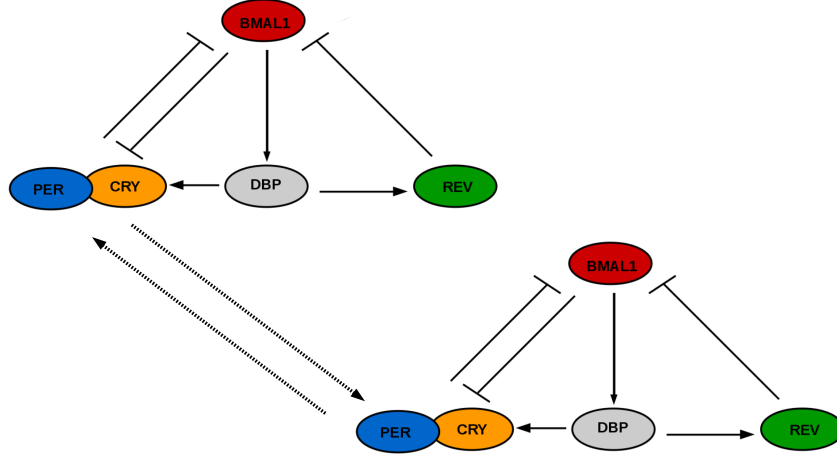
3

Figure 1: Diffusive coupling between two circadian clocks through the complex PER:CRY.

and thus a lower rate (εV_D) of complex PER:CRY formation (Table 2 in Appendix shows the correspondence between ε values and periods.)

Several earlier studies have shown that the *Per2* gene is responsive to multiple signaling pathways both in the SCN and in peripheral organs ([22, 4]). Interestingly, recent experimental data [12] shows that paracrine signaling downregulates *Dbp* and upregulates *Per2* expression, suggesting that gene *Per2* is an early responder to intercellular clock communication. In this paper, we will assume that this communication is represented by a direct diffusive action on the complex PER:CRY variable P. Although a highly simplified representation, it avoids the introduction of new uncalibrated variables into the model, and allows us to continue our analytical study. The resulting coupled model is:

$$
\begin{aligned}
\dot{B}_i &= V_R h^-(R_i) - \gamma_B B_i P_i, \\
\dot{D}_i &= V_B B_i - \gamma_D D_i, \\
\dot{R}_i &= V_D D_i - \gamma_R R_i, \\
\dot{P}_i &= \varepsilon_i V_D D_i - \gamma_B B_i P_i + k(P_j - P_i),
\end{aligned}
\tag{3}
$$

In the next sections, we will analyze the effect of ε and k in the coupled network, assuming a weak coupling rate [15] and a wider interval for the circadian periods $\varepsilon_{min} < \varepsilon < \varepsilon_{max}$.

2.2 Synchronization of two systems

In a first step we will study the synchronization of two systems (using $\varepsilon_1 = 1$ and $\varepsilon_2 = \varepsilon$), as a function of the factor ε and the coupling strength k. To do this, we compute the total difference between the variables, $|r| = \sqrt{r_B^2 + r_D^2 + r_R^2 + r_P^2}$, with $r_B = B_1 - B_2$, $r_D = D_1 - D_2$, $r_R = R_1 - R_2, r_P = P_1 - P_2$.

The total difference $|r|$ will increase with the perturbation $(1 - \varepsilon)$ (mutation "strength") and decrease with the coupling strength k. Fig. 2 illustrates the opposite effects of period differences and coupling strength on the error. In the case of equal periods (i.e., $1 - \varepsilon = 0$), the error converges to zero and the two clocks synchronize exactly, while the coupling strength cannot guarantee exact synchronization.

To further study the role of coupling in maintaining cell synchronization and the capacity of the cells to synchronize, we performed two types of simulations to calculate the amount of time
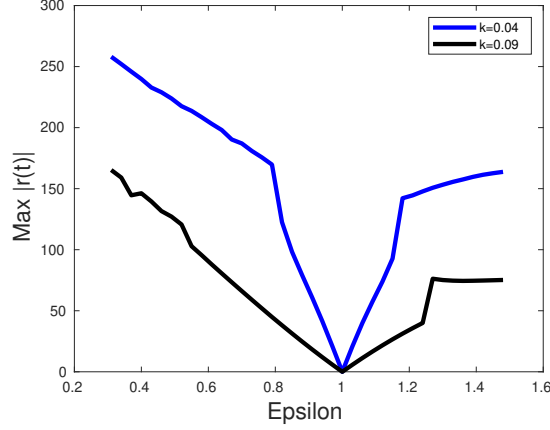
Figure 2: Maximum of the total difference $|r| = \sqrt{r_B^2 + r_D^2 + r_R^2 + r_P^2}$ as a function of ε, for two coupled systems (3). The parameters are those listed in (2).
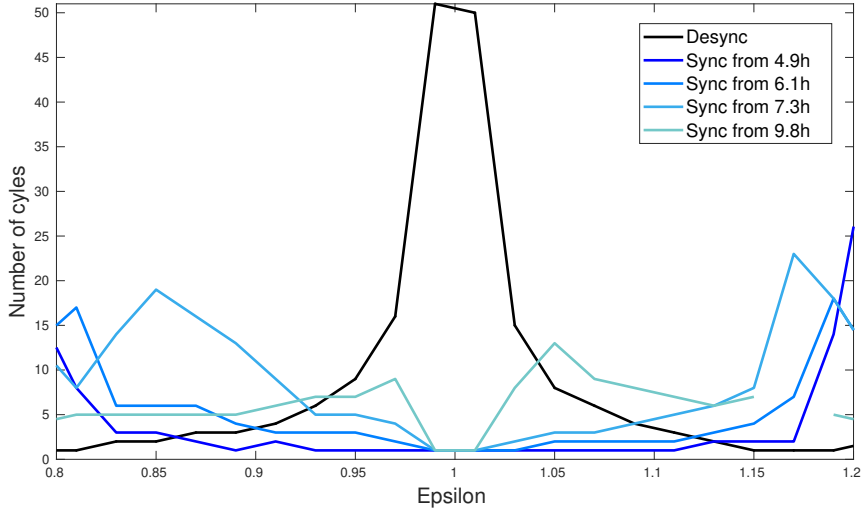

Figure 3: Number of circadian cycles needed for desynchronization and synchronization of two oscillators. Desynchronization (black curve): the two oscillators start from a point were their phase difference is smallest and the coupling is turned off. Synchronization (blue curves): the two oscillators start from a point where their phase difference is either $0.2\tau_1 = 4.9h$, $0.25\tau_1 = 6.1h$, $0.3\tau_1 = 7.3h$, or $0.4\tau_1 = 9.8h$, with $\tau_1 = 24.5h$ and the coupling is turned to $k = 0.04$. In both cases, the oscillators are considered synchronized while their phase difference is lower than $0.15\tau_1 = 3.6h$.

needed to desynchronize two cells once coupling is disabled or, conversely, to calculate the time needed to synchronize cells that start with some phase difference. (Throughout this Section, we compute the oscillators phases relative to the crossing of threshold value k_R by variable R, as it decreases.) Fig. 3 shows the number of circadian cycles needed to desynchronize or synchronize two cells, as one of the periods varies in terms of ε. Unsurprisingly, the time needed to desynchronize cells increases in an exponential form as the two oscillator periods become closer (black curve). More interestingly, the form of the synchronization curve highly depends on the initial phase difference between the two oscillators. For phase differences up to ≈ 8 hours, the number of cycles to synchronization decreases with the difference between

periods. For low initial phase differences (about 5 to 6 hours), the time to synchronization is less than six circadian cycles for two cells with periods $\tau_1 = 24.5h$ and $24.8 < \tau_2 < 25.5$ (that is, $0.85 < \varepsilon < 0.95$). For a higher initial phase difference of about 7.3h, the two cells need from 20 to 5 cycles to synchronize. Finally, for very high initial phase differences (around 10 hours, see lighter blue curve) the trend is inverted, since synchronization times are around five circadian cycles for $25.2 < \tau_2 < 25.5$ (that is, $0.85 < \varepsilon < 0.9$) and then increase to about seven cycles for $\tau_2 = 24.8$ (or $\varepsilon = 0.95$).

Our simulations evoke an observation on SCN clocks, for which it has been reported that the role of neuropeptide VIP (a factor implicated in cell communication) in synchronization is dose dependent, with a low VIP leading to synchronization but a high VIP leading to desynchronization [3].

3 Characterization of circadian cycle timing

In order to better understand how the coupling mechanism works, the effect of the period differences (characterized by ε) and the coupling strength k on the synchronization, we will divide the circadian cycle into six different stages, based on the dynamics of the CLOCK:BMAL1 / PER:CRY mutual inactivation. To do this, the nonlinear terms of model (1) are simplified to create a piecewise linear model [7] that partitions the state space into six different regions. The time spent by the orbit in each of these regions can then be explicitly calculated in terms of the system's parameters and switching conditions, providing estimates for the duration of each stage. A computational study shows the duration of each stage and their re-organization in the coupled network.

3.1 A piecewise linear clock model

There are two nonlinear terms in system (1). First, let's consider the decreasing Hill function $f(R) = V_R \frac{k_R^4}{k_R^4 + R^4}$. This class of functions is often simplified by a step function [7]:

$$f(R) \approx \begin{cases} 0, & R > k_R \\ V_R, & R < k_R \end{cases} \tag{4}$$

The second nonlinear term is the common degradation or inactivation of the complexes CLOCK:BMAL1 and PER:CRY, that is, $-\gamma_B BP$. As the oscillator performs one full cycle, this term goes through several well marked conditions (see Fig. 4). Define B^* and P^* to be low levels of reference for the variables B and P, respectively. Consider also B_{high} and P_{high} to be high levels of reference for those variables. Let B_{max} and P_{max} denote their maximal values. These reference values define a family of intervals in B and P ($[0, B^*], [B^*, B_{max}]$ and $[0, P^*]$, $[P^*, P_{high}]$, $[P_{high}, P_{max}]$) where the CLOCK:BMAL1 and PER:CRY common inactivation term can be simplified by setting either B or P to be at their *low* or *high* reference values.

Notice that while B is approximately constant at its low level B^*, or when P is very large ($P > P_{high}$), the two terms $\gamma_B BP$ and $f(R)$ have similar values, so they add up approximately to 0 in the B equation. This suggests the following simplification:

$$\gamma_B BP \approx \begin{cases} 0, & R > k_R \text{ and } B < B^* \\ V_R, & R < k_R \text{ and } P > P_{high} \end{cases} \tag{5}$$
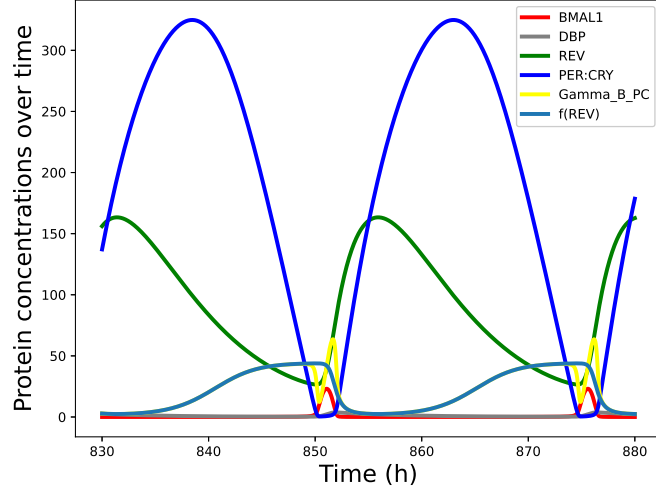
Figure 4: Protein concentrations over time and $\gamma_B BP$ and $f(R)$ curves.

To approximate $\gamma_B BP$ in the other cases, we adopt the following criterion: for intermediate levels of P, we assume that the inactivation term is dominated by the B dynamics with P constant, while for very low P, the opposite scenario holds. Taking into account the phase opposition between B and P, we expect B to be close to its maximum value when $P < P^*$. We thus propose the following piecewise linear approximation for $\gamma_B BP$:

$$\gamma_B BP \approx \begin{cases} 0, & R > k_R, B < B^* & \text{Stage 1} \\ V_R, & R < k_R, P > P_{high} & \text{Stage 2} \\ \gamma_B BP^*, & R < k_R, P^* < P < P_{high} & \text{Stage 3} \\ \gamma_B B_{max}P, & R < k_R, P < P^* & \text{Stage 4} \\ \gamma_B B_{max}P, & R > k_R, B > B^*, P < P^* & \text{Stage 5} \\ \gamma_B BP^*, & R > k_R, B > B^*, P > P^* & \text{Stage 6} \end{cases} \quad (6)$$

These conditions cover all the state space and ensure positivity of the piecewise linear system composed of (1)-(4)-(6). To simulate this system we need to provide suitable values for the reference levels.

To estimate B_{max}, consider the steady state obtained when transcription is activated and the degradation term is fixed at $\gamma_B BP^*$:

$$\dot{B} \approx V_R - \gamma_B BP^* \Rightarrow V_R - \gamma_B B_{max}P^* = 0 \Leftrightarrow B_{max} = \frac{V_R}{\gamma_B P^*}.$$

To estimate the low level P^*, consider the cycle's phase opposition property and assume that both B and D reached their maximum values, and P is produced at a rate $\varepsilon V_D D_{max}$:

$$\dot{D} \approx V_B B_{max} - \gamma_D D \Rightarrow V_B B_{max} - \gamma_D D_{max} = 0 \Leftrightarrow D_{max} = \frac{V_B B_{max}}{\gamma_D}$$

$$\dot{P} \approx \varepsilon V_D D_{max} - \gamma_D B_{max}P \Rightarrow \varepsilon V_D D_{max} - \gamma_D B_{max}\bar{P} = 0 \Leftrightarrow \bar{P} = \frac{\varepsilon V_D D_{max}}{\gamma_B B_{max}} = \frac{\varepsilon V_D V_B}{\gamma_B \gamma_D}.$$

For a safer estimate we consider $P^* = \bar{P}/4$, so that

$$P^* = \frac{\varepsilon V_D V_B}{4\gamma_B \gamma_D} \quad \text{and} \quad B_{max} = \frac{4V_R \gamma_D}{\varepsilon V_D V_B}$$

7

In contrast, there is no obvious way to estimate a suitable non-zero value for B^*, so we choose a fixed low value, $B^* = 0.01$ for the simulations in this paper. Set $B_{high} = B_{max}$ since a distinction is not required between them. Finally, P_{max} is not used explicitly but an intermediate value for P must be fixed. In the current simulations, we use an appropriately high value within the system's parameters and set $P_{high} = V_R$.

Fig. 5 shows oscillations of the 4 proteins of the piecewise linear model (1)-(4)-(6, as well as the duration of each stage (black straight lines), with parameter set (2). We observe that, depending on the parameter set, the system may not go through all six stages.
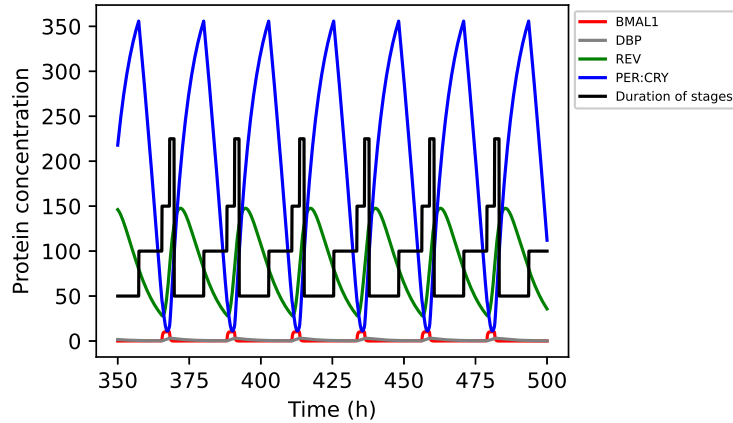

Figure 5: Protein concentrations over time and stages duration, for the piecewise linear model. The stages are represented by the black straight lines, corresponding to the ordinates 50, 100, 150, 175, 200 and 225, respectively.

3.2 A partition of the circadian cycle

Through the simplification of the continuous model (1) into a piecewise affine model we analyse the circadian cycle as a sequence of six main stages, based on the repression of CLOCK:BMAL1 by REV and the dynamics of the mutual degradation/sequestration between CLOCK:BMAL1 and PER:CRY. Our stages can be compared to the common circadian time (CT) description [21], which is based on the circadian transcriptional landscape in the mouse liver. This means that night hours (from CT12 to CT0/24) correspond to the mouse activity and feeding while the daylight hours (from CT0 to CT12) correspond to the resting and fasting phase. In this context, we find that the circadian night is divided into two stages, both characterized by a decreasing or low concentration of CLOCK:BMAL1 and the common degradation term either modulated by CLOCK:BMAL1 dynamics (stage 6) or at a very low level (stage 1).

The circadian daylight interval is divided into approximately three stages. An early day (stage 2) corresponding to a very high PER:CRY level, which imposes a high but saturated common degradation term, and CLOCK:BMAL1 de-repressed. The beginning of this stage would approximately correspond to the beginning of the circadian time count CT0. The second daylight stage (3) corresponds to CLOCK:BMAL1 augmentation as PER:CRY decreases with their degradation modulated by the dynamics of CLOCK:BMAL1. In the third daylight stage (4) PER:CRY is now at a low level while CLOCK:BMAL1 is still increasing, but their common degradation term is now modulated by PER:CRY dynamics. The end of this stage would correspond to middle circadian time (CT12). Finally, there is a day-to-night transition (stage 5), where REV has reached its switching value and repression of CLOCK:BMAL1 is turned on.

Table 1: Characterization of the six circadian time stages based on the mutual CLOCK:BMAL1 and PER:CRY inactivation dynamics.

Stage	1	2	3	4	5	6
Circadian time	night	early day CT0$\rightarrow$	day	day $\rightarrow$ CT12	day/night transition	night
CLOCK:BMAL1 (B)	low $B < B^*$	low $B > 0$	increasing $B > 0$	high $B > 0$	high $B > B^*$	decreasing $B > B^*$
PER:CRY (P)	increasing $P > 0$	high $P > P_{high}$	decreasing $P^* < P < P_{high}$	low $P < P^*$	low $P < P^*$	increasing $P > P^*$
Common degradation	negligeable	satured by P	modulated by B	modulated by P	modulated by P	modulated by B
Repression of CLOCK:BMAL1	on $R > K_R$	off $R < K_R$	off $R < K_R$	off $R < K_R$	on $R > K_R$	on $R > K_R$

3.3 Duration of each cycle stage in terms of the system's parameters

The advantage of the piecewise linear approximation is to allow the explicit computation of a solution for four of the six cycle stages and hence also an expression for these four stages duration in terms of the parameters. We can express the duration of stages 6,1,2, and 3 in terms of the parameters, but expressions for stages 4 and 5 are more complex to derive. However, in all our examples, stages 4 and 5 have very short duration (lower than about 2 hours).

For stage 6, we have the following equation for B: $\dot{B} = -\gamma_B B P^*$ whose analytical solution is: $B(t) = e^{-\gamma_B P^*(t-t_0)} B(t_0)$. Letting (t_3, t_6) denote the times at which the cycle end stage 3 and 6, respectively, we assume that $B(t_3) = B_{max} = V_R/(\gamma_B P^*)$ and $B(t_6) = B^*$. So, recalling $P^* = \varepsilon V_D V_B/(4\gamma_B \gamma_D)$, obtain

$$B(t_6) = e^{-\gamma_B P^*(t_6-t_3)} B(t_3) \quad \Rightarrow \quad t_6 - t_3 = -\frac{4\gamma_D}{\varepsilon V_D V_B} \ln\left(\frac{\varepsilon B^* V_D V_B}{4 V_R \gamma_D}\right) \tag{7}$$

Since ε represents *Cry2* knockout, as ε decreases the period of the system increases. This expression shows that duration of stage 6 also increases with the effectiveness of *Cry2* knockout.

In a similar way, we can compute the duration of stages 1, 2 and 3:

$$t_1 - t_6 = -\frac{1}{\gamma_D} \ln\left(\frac{D(t_1) - \frac{V_B B^*}{\gamma_D}}{D(t_6) - \frac{V_B B^*}{\gamma_D}}\right) \tag{8}$$

$$t_2 - t_1 = -\frac{1}{\gamma_D} \ln\left(\frac{D(t_2) - \frac{V_B B^*}{\gamma_D}}{D(t_1) - \frac{V_B B^*}{\gamma_D}}\right) \tag{9}$$

$$t_3 - t_2 = -\frac{1}{\gamma_B P^*} \ln\left(\frac{B(t_3) - \frac{V_R}{\gamma_B P^*}}{B^* - \frac{V_R}{\gamma_B P^*}}\right) \tag{10}$$

Duration of stage 6 depends only on the parameters whereas duration of the other stages ($k = 1, \ldots, 5$) depends also on the values reached by D and B at the beginning ($D(t_{k-1})$, $B(t_{k-1})$) or at the end ($D(t_k)$, $B(t_k)$) of stage k, that we don't necessarily know how to estimate.

Notice that stages 6, 1 and 2 follow each other in this order. Since the equation of D is the same for all stages, during stages 1 and 2, its solution is

$$D(t) = e^{-\gamma_D(t-t_0)}\left(D(t_0) - \frac{V_B B^*}{\gamma_D}\right) + \frac{V_B B^*}{\gamma_D} \tag{11}$$

The lower level D^* of D is reached when $B = B^*$ so we can estimate it :

$$\dot{D} \approx V_B B^* - \gamma_D D \Rightarrow V_B B^* - \gamma_D D^* = 0 \Leftrightarrow D^* = \frac{V_B B^*}{\gamma_D}$$

So, as $D(t_0) > \frac{V_B B^*}{\gamma_D}$, $D(t)$ is decreasing during stages 1 and 2, so that $D(t_6) > D(t_1) > D(t_2)$.

Fig. 6 shows the duration of each stage as a function of ε. For parameter set (2), the piecewise linear system doesn't go through the stages 4 and 5. With respect to ε, stage 6 decreases strongly then stabilizes, stage 3 increases then stabilizes, stage 1 increases for very low ε then decreases. Stage 2 seems to increase close to linear. Let's focus now on the duration of the period: because of the strong decrease of stage 6, it decreases, then because of the increase of stage 2 and the stabilization of stages 3 and 5, it increases. More specifically, it is interesting to
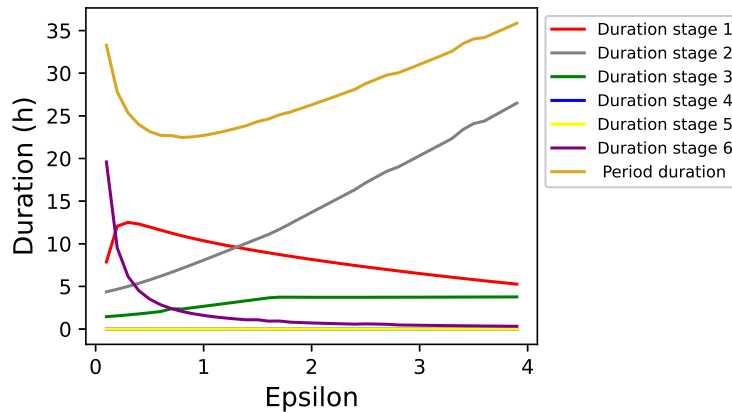

Figure 6: Duration of each stage as a function of ε

compare the model behavior for $\varepsilon < 1$ with *Cry2* knockout cells: lower ε values represent more effective knockouts, with less available protein CRY2. *Cry2* knockouts have higher periods and amplitudes [15] and our model shows that the period increases with the effectiveness of the knockout. Moreover, our model shows that the longer period is due to a longer duration of stage 6 corresponding to a longer end of the day, in agreement with the property that *Cry2* deficient mice represent models of "eveningness" [9] (showing activity patterns later in the day).

4 Circadian stages and period duration in a mixed cell population

To study the coupling dynamics in a cell population with mixed periods, we now consider the continuous system (3) with $\varepsilon_1 = 1$ and $\varepsilon_2 = \varepsilon$, to reproduce two coupled oscillators with different periods. To further analyse the dynamics, we measure the duration of the six stages for each oscillator, according to the conditions summarized in Table 1. Fig. 7 shows the stage and period durations of the coupled system, as a function of ε, for two values of the coupling strength k.

As expected, a higher coupling constant allows synchronization of the periods for a wider interval around $\varepsilon = 1$. For $\varepsilon < 1$, this simulation evokes the mixture between *Cry2* knockout and wild type cell populations performed for instance in [15] or [12]. The period becomes longer as $\varepsilon < 1$ decreases (check thin dashed lines, uncoupled oscillator 2), as is the case in *Cry2* knockout cells. The mixture of wild type and *Cry2* knockout cells is represented by the
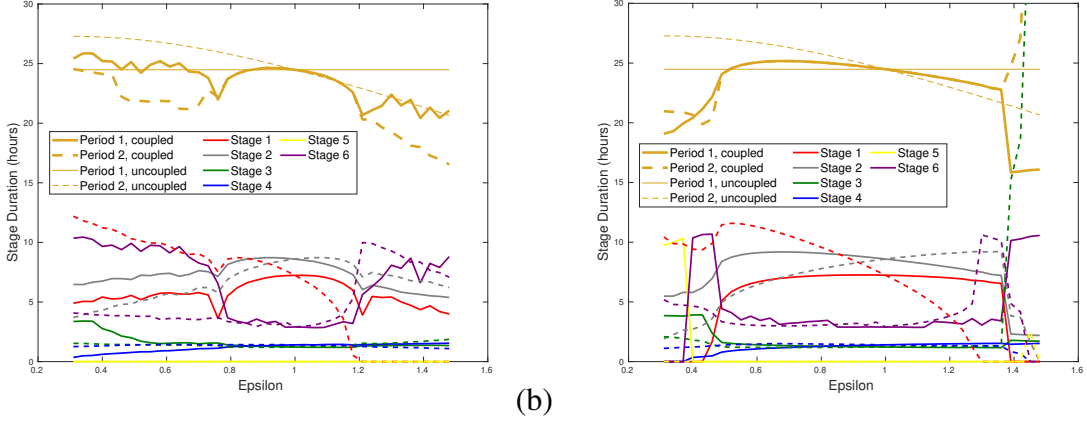
Figure 7: Duration of stages and period for system (3) as a function of ε. (a) k=0.04; (b) k=0.09. In both panels, the solid lines represent oscillator 1 ($\varepsilon = 1$) and the dashed lines represent oscillator 2 ($\varepsilon \neq 1$). The thin solid and dashed yellow lines represent the periods of the oscillators before coupling.

coupled oscillators solid and dashed thick lines, respectively ($\varepsilon < 1$). In this case, we see that the longer periods are shortened by up to 2 hours (dashed line) while the wild type cells remain at approximately the same period (solid line) in a small neighborhood of $\varepsilon = 1$, in good agreement with the recent observations by [12] (Figure 1 H,J in this reference).
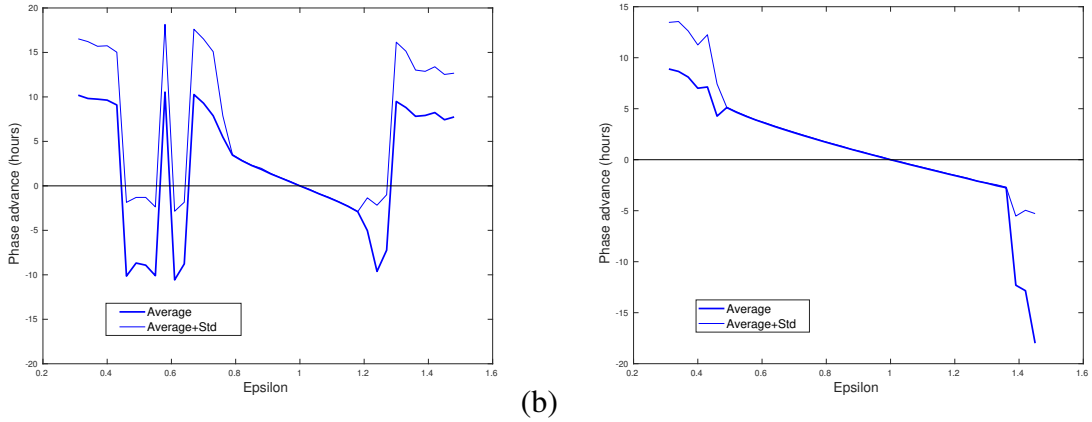

Figure 8: Phase advance of oscillator 2 ($\varepsilon \neq 1$) over oscillator 1 ($\varepsilon = 1$), as an average over about 50 periods. (a) $k = 0.04$; (b) $k = 0.09$. Thin lines represent average plus standard deviation.

Although amplitudes and periods of both oscillators remain similar, notice that the duration of each stage may differ substantially from one oscillator to the other (compare same-color solid and dashed lines in Fig. 7): the two oscillators spend different amounts of time in different stages, while remaining synchronized on the full period. Fig. 8 confirms that, in a close neighborhood of $\varepsilon = 1$, the coupled oscillators have essentially the same periods but with a phase difference, in particular the variables' peaks are not reached simultaneously.

To further understand the mechanisms leading to the distinct duration of stages 1 and 2 in the two coupled oscillators, we first identified the entry and exit points from each stage and then identified and compared the dominant processes involved in each of the stages. In agreement with (6), stage 1 is completely defined by the value of BMAL1, since both entry and exit points

from this stage correspond to the crossing of threshold B* by BMAL1, as this protein is either decreasing (entry to stage 1) or increasing (exit to stage 1) (see Fig. 9 (a)). The entry and exit to stage 2 are defined by REV and PER:CRY, respectively. The oscillators enter into stage 2 when REV crosses its activation level k_R, while decreasing (see Fig. 9 (b)) and exit stage 2 when PER:CRY crosses its high level P_{high} while decreasing (see Fig. 9 (c)).
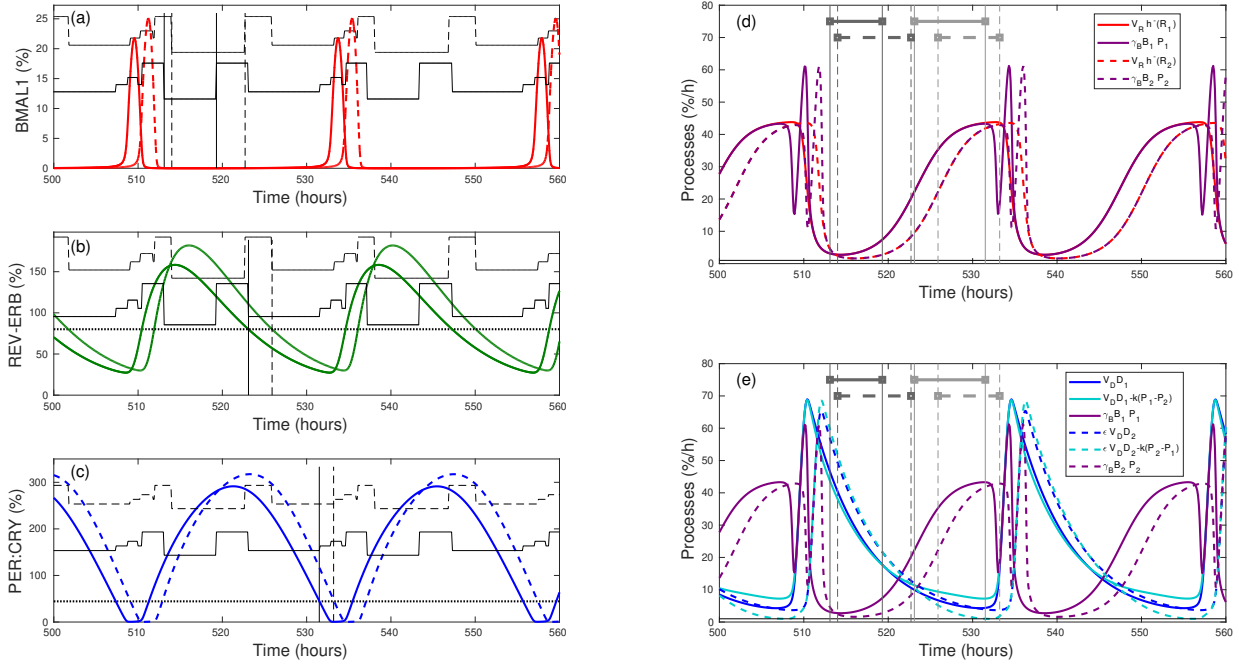

Figure 9: Dynamics of two coupled oscillators with $k = 0.04$ and $\varepsilon = 0.82$. Oscillator 1 is shown in solid curves, oscillator 2 is shown in dashed curves. The uncoupled system periods are $\tau_1^u = 24.5h$ and $\tau_2^u = 25.5h$, while the coupled periods are $\tau_1^c = \tau_2^c = 24.4h$. (a)-(c) Times series of variables B (red), R (green), and P (blue). The solid and dashed black horizontal lines denoted the length of the six stages. The vertical lines denote the beginning and ending of stages 1 and 2. (d)-(e) Times series of the main processes at play in the equation of the systems: synthesis of B and P ($V_R h^{-1}(R_j)$ and $V_D D_j$), their mutual degradation term ($\gamma_B B_j P_j$), and the effect of coupling (plotted as $V_D D - k(P_i - P_j)$).

We then compared the strength of the different processes during the two stages (see Fig. 9 (d)-(e)) It follows that during stage 1, repression of BMAL1 by REV is high and the mutual degradation of BMAL1 and PER:CRY is at a low level. The dominant process during stage 1 is clearly the production term of PER:CRY, $V_D D$. Comparison of the dark and light blue curves of Fig. 9 (e), shows that the coupling term is also negligible during this stage. This last observation indicates that the two oscillators are operating in a close to uncoupled mode and therefore the longer period oscillator naturally shows a longer duration of stage 1.

Conversely, during stage 2, the opposite happens, with low repression of BMAL1 by REV and the mutual degradation of BMAL1 and PER:CRY at high level is now the dominant process (see Fig. 9 (d)). Also, during stage 2, the coupling term is at its highest strength, as can be seen by its effect on P:C dynamics: the coupling term increases (resp., decreases) the production rate of the shorter (resp., longer) period oscillator. This leads to the longer period oscillator decreasing PER:CRY levels faster and hence reaching the threshold P_{high} faster than expected

relative to the uncoupled oscillator. Inversely, the shorter period oscillator reaches P_{high} slower than expected. Thus, during stage 2, the coupling term is largely responsible for decreasing the difference between the two periods by imposing a shorter duration of this stage for the longer period oscillator and a longer duration of this stage for the shorter period oscillator.

These conclusions are confirmed by Fig. 10, which show that the duration of stage 1 is roughly the same in the case of coupled or uncoupled oscillators in a small neighborhood of $\varepsilon = 1$. In contrast, the duration of stage 2 for oscillator 2 decreases significantly from the uncoupled to coupled situation (for $\varepsilon < 1$), while it increases slightly for oscillator 1. The synchronization dynamics between two oscillators along the circadian cycle is summarized in Fig. 11, which highlights the dominant processes at each stage.
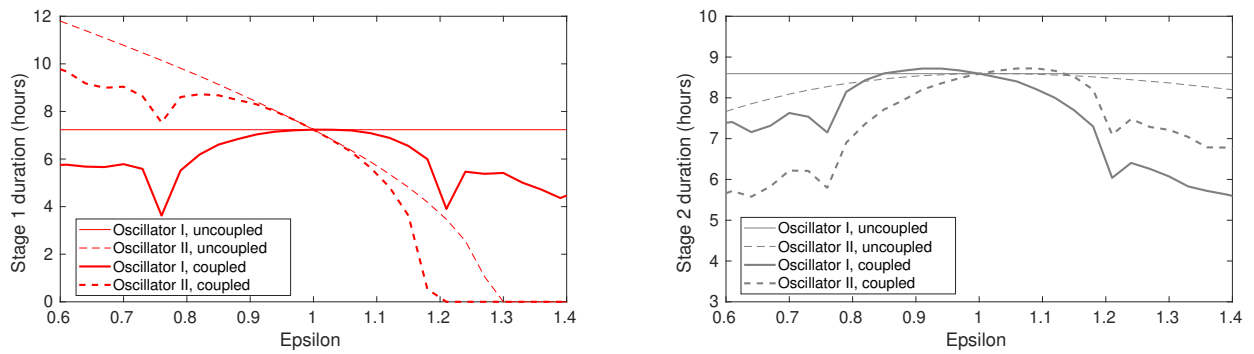

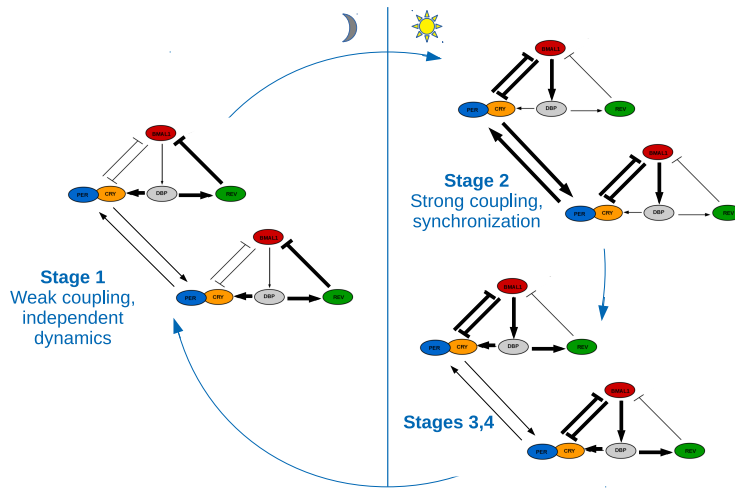Figure 10: Comparison of duration of stages 1 and 2 for the coupled and uncoupled oscillators.

Figure 11: Dominant processes throughout one circadian cycle. During stage 1 (circadian night) the two oscillators evolve in a weakly coupled mode, each oscillator following its individual natural period. Concentrations of PER:CRY and REV increase overall. During stage 2 (circadian early day), coupling is at its strongest level, leading to the adjustment of the two oscillators periods, with a shorter stage 2 duration for the longer period oscillator.

5 Clock synchronization in response to time-restricted feeding

So far, we have studied the coupling between two oscillators. However, the study of cell periods in a mixture of wild type and *Cry2* knockout cells suggests that hepatocytes are coupled in clusters of 5 to 10 cells (see [15]). In liver lobules, cells are organised in parallel rows. We tested 5 distinct topologies (star, all-to-all, ring, rows and chain) to represent different patterns of exchanges between the cells. We report our results on star topology (see Fig. 12).
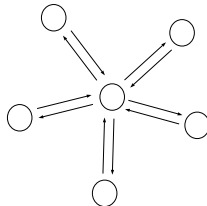

Figure 12: Star topology

In this section, we use our clock model to study the relevance of peripheral clock coupling in the response to different regimes of time-restricted feeding in liver circadian clocks of mice. Recent *in vivo* experiments by Sinturel *et al.* [20] show that coherent oscillations are maintained in the liver of mice devoid of a functional SCN or having a clock exclusively in hepatocytes. We designed a computational study to reproduce the experimental protocol in these experiments, consisting of feeding mice (with and without SCN) ad libitum for about 20 days, then alternating periods of fasting and feeding (of 12 hours each) for about 20 days before feeding them again ad libitum. Circadian oscillations were monitored longitudinally in free-living animals thanks to PER2::luciferase reporter. The experiments show that during ad libitum intervals, oscillations in mice without SCN are damped. However, a 12 hour alternance between eating and fasting intervals permits rhythmic and increasing oscillations in peripheral organs.

After food intake, glycemia increases and causes the pancreatic β-cells to secrete insulin [5]. Glucose and insulin levels are strongly linked and that is why we model the food intake with insulin ($I(t)$), added in the CLOCK:BMAL1 equation:

$$\dot{B} = V_R h^-(R) - \gamma_B BP + I(t) \tag{12}$$

We consider a cluster of 8 cells with initial periods taken randomly between 23.01h and 26.32h ($0.7 \leq \varepsilon \leq 1.2$), coupled in a diffusive way through PER:CRY ($k = 0.04$) in a star topology. To model ad libitum food intake in SCN lesioned mice (arrhythmic feeding situation), we let insulin be at a constant but low level $I(t) = 2\%/h$, throughout the first 20 days. To model time-restricted feeding, we add 2-hour pulses of insulin with high amplitude $I(t) = 13\%/h$, once every circadian cycle. As the peak of insulin lasts about 2 hours and using results of [2], the 2 hour pulse is applied from CT5 to CT7 during ten days and then from CT17 to CT19 during the next ten days. This schedule corresponds to the restricted access to the food during either the resting or activity phase respectively as in [20].

Fig. 13 reports the average concentration of PER:CRY among the 8 cells, $\bar{P}(t) = \frac{\sum_{i=1}^{8} P_i(t)}{8}$, throughout the sequence of $20 + 10 + 10 + 20$ days. To check the effect of coupling, we performed exactly the same protocol to a cluster of 8 individual cells without any coupling
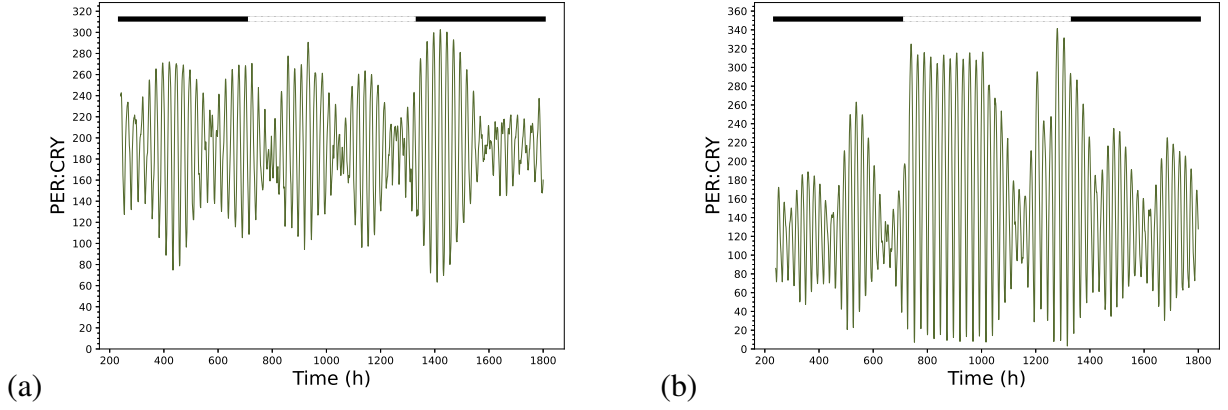
Figure 13: Average PER:CRY concentrations over time for ad libitum feeding (black bands) or time-restricted feeding (white bands), over a cluster of 8 cells with different periods ($\tau_1 = 24.11h$, $\tau_2 = 23.48h$, $\tau_3 = 23.55h$, $\tau_4 = 26.29h$, $\tau_5 = 26.17h$, $\tau_6 = 26.15h$, $\tau_7 = 24.95h$ and $\tau_8 = 24.58h$). (a) Without coupling and (b) Star topology and $k = 0.04$.

(Fig. 13(a)) or with diffusive coupling, in a star topology, with weak coupling strength $k = 0.04$ (Fig. 13(b)). Comparison of Figs. 13 (a) and (b) shows that, during periods of time-restricted feeding, oscillations are rhythmic and their amplitude increases strongly, especially in the case of weakly coupled cells. For a more detailed analysis of these signals, we performed Fast Fourier Transforms (FFT) for the ad libitum intervals and the time-restricted feeding intervals without and with coupling ($k = 0.04$) (see Fig 14, blue and orange curves, respectively).

The FFT analysis highlights several aspects. First, in the intervals of time-restricted feeding (see Fig 14 (b)), the cluster of uncoupled cells show two small amplitude peaks around 22h and 25h. Conversely, the cluster of coupled cells shows only one well defined peak around 23h, with at least a two-fold higher magnitude. This observation indicates that the coupled cluster has the capacity to produce a significant coherent signal under the time-restricted feeding regime, corresponding well to the experimental results of [20]. A clear contrast is presented by the uncoupled cluster, unable to generate coherent oscillations and showing two low amplitude periods, conform to those present in the 8 individual cells.

A second observation is that the main peak representing ad libitum feeding (see Fig 14 (a)) is centered around 25h for the uncoupled cluster, while it has a lower period for the coupled cluster.

To complete these observations, we analyzed the amplitudes of the 3 main peaks of the FFT in terms of different values of insulin, for ad libitum feeding periods (values of insulin between 0.5 and 5) and time-restricted feeding periods values of insulin between 11 and 15.5) separately (see Fig 15), with and without coupling.

In the intervals of time-restricted feeding, the coupled cluster shows a peak with a significantly higher amplitude (see Fig 15(b), dashed red line) than the other peaks, suggesting that the cells synchronize over the same period. At the opposite, for uncoupled clusters all peaks have comparable amplitudes indicating that several different periods are similarly represented, thus uncoupled cells are weakly or not synchronized. In the intervals of ad libitum feeding, peaks have similar amplitudes, no matter whether there is coupling or not, suggesting weak synchronization.

Comparison between the amplitude of the peaks of the FFT between ad libitum feeding and time-restricted feeding for a coupled system (see Fig 15) shows that the main peak of time-restricted feeding is significantly higher than the main peak of ad libitum feeding, in agreement with the experimental results of [20] (Fig.2, F). There is not such difference between the peaks

15

of ad libitum feeding and time restricted feeding for an uncoupled system, again suggesting a lack of synchronization in uncoupled cells.

Remarkably, our simulations are in agreement with experimental results for mice without SCN [20], suggesting that small clusters of weakly coupled cells are important elements for achieving coherence and synchronization of peripheral clocks.
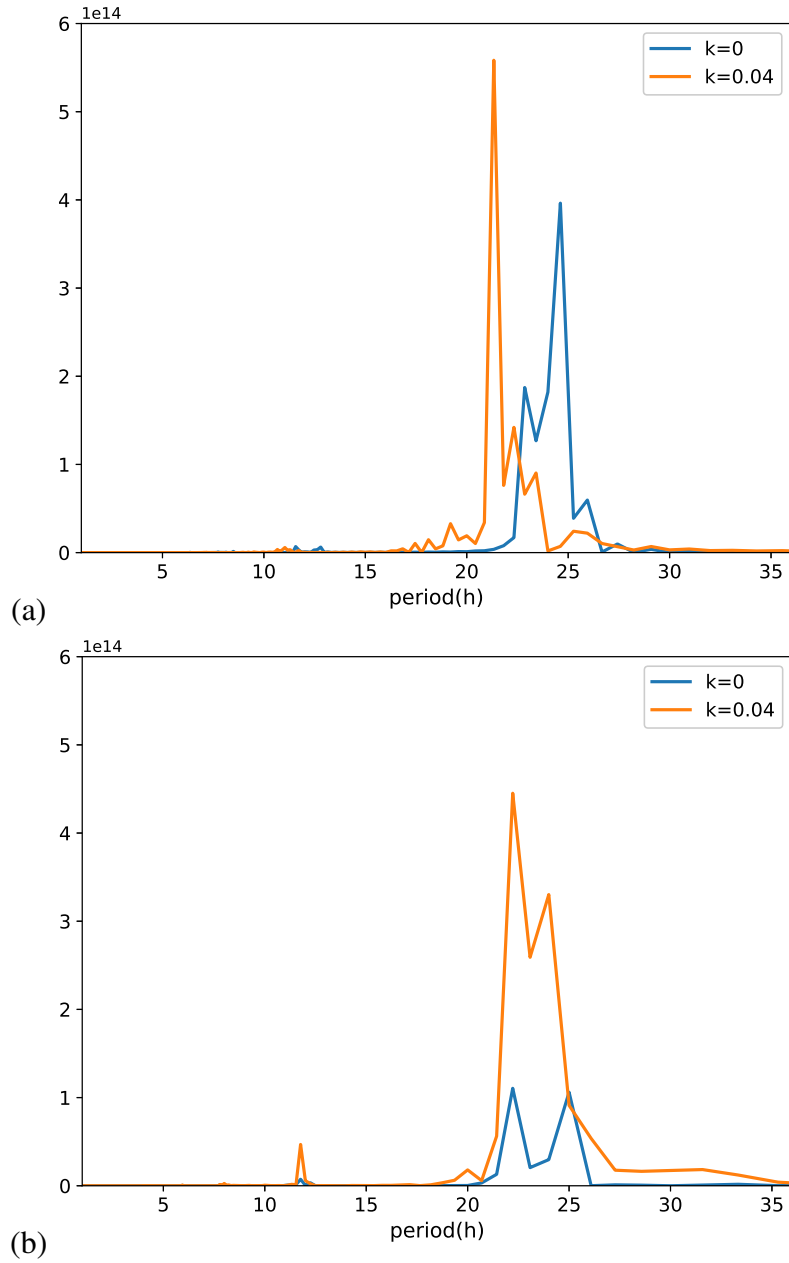

Figure 14: FFT analysis of Fig. 13. Blue curve: Without coupling. Orange curve: Star topology and $k = 0.04$. (a) Periods during ad libitum feeding; (b) Periods during time-restricted feeding.

6 Discussion

This theoretical and computational study was motivated by recent experimental observations suggesting that intercellular coupling between circadian clocks occurs in peripheral organs such
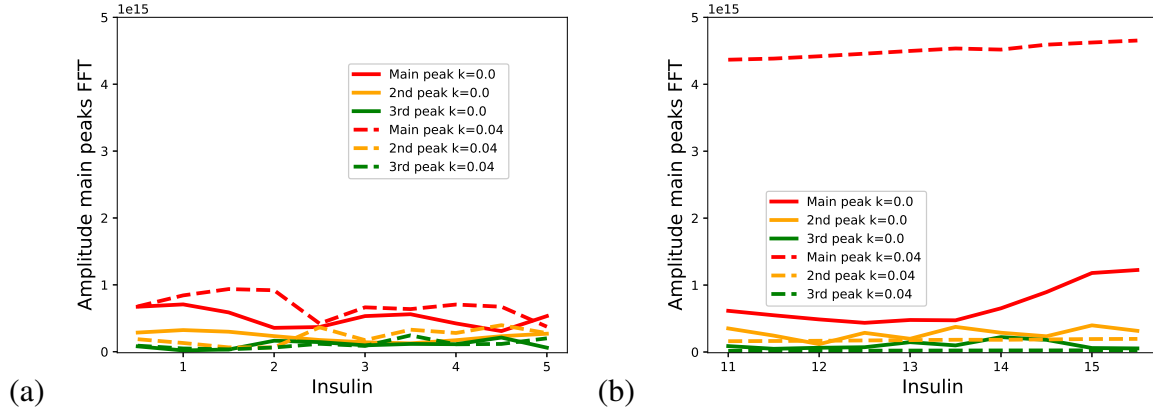
Figure 15: Amplitudes of the 3 main peaks of FFT for k=0 (solid lines) and k=0.04 (dashed lines) in terms of insulin values. (a) Ad libitum feeding; (b) Time-restricted feeding.

as the liver and contributes to maintain coherent oscillations in the absence of the SCN master clock. We constructed a network of coupled peripheral clocks to provide an early analysis of some aspects of the coupling dynamics.

Using a validated transcriptional model of the clock. Our model of the mammalian circadian clock was developed in previous work, calibrated with data from mouse fibroblasts, and validated on a number of applications (for instance, on the interactions between the mammalian clock and cell cycle). This model, with its validated set of physiological parameters, constituted a solid basis for our coupled network and its analysis, a clear advantage relative to generalist phase models used in many studies. Namely, this model allowed us to represent populations of cells with either longer or shorter periods, by tuning only one parameter (ε).

A partition of circadian cycle into six stages to characterize synchronization dynamics. To more closely analyze the coupling dynamics, we devised a partition of the circadian cycle based on the repression of BMAL1 and the common inactivation between the complexes CLOCK:BMAL1 and PER:CRY. In this way we obtain a circadian cycle with six stages, each representing one part of the circadian day and its length characterized by the system's parameters. This partition was used to study the coupling process in a mixture of wild type and longer period $Cry2^{-/-}$ cells. Comparison of the clock periods with or without coupling shows that the longer period $Cry2^{-/-}$-type cells shorten their periods in a coupled network, while wild type cells do not greatly change their periods, a result in very good agreement with the recent work of [12].

Our results highlight the fact that two coupled oscillators may be synchronized in period but have quite different duration for each stage (Fig. 9). Analysis of the main processes (Fig. 11) shows that, during stage 1 (circadian night) the coupling term is negligible, and the oscillators operate near to uncoupled mode, with the longer period oscillator naturally exhibiting a longer stage 1. Conversely, during stage 2 (circadian early day), the coupling is at its strongest level and succeeds in balancing the two periods by shortening the longer period oscillator.

Synchronization in a cluster of cells in response to time-restricted feeding. In the liver, communication between hepatocytes spreads to clusters of less than 10 neighbor cells, under weak coupling [15]. We used our model to represent these cell clusters as observed in liver lobules, and simulated both uncoupled or coupled clusters with high period variability (between 23 and 26.5 hours), to study the average PER:CRY signal in response to either ad libitum or time-restricted feeding. Our simulations indicate that both timed food intake and intercellular coupling are determinant factors for the PER:CRY amplitude and period of oscillations

17

(Fig. 13). Moreover, both factors are needed to reproduce the experimental observations, as shown by comparison of results with and without network coupling (Fig. 14 (a) and (b) and Fig. 15). The model with network coupling reproduces more faithfully than the one without coupling the recent experiments showing that hepatocyte clocks still synchronize in mice devoid of a functional SCN. This comparison of model and data thus suggests that coherence and synchronization of peripheral clocks is possible thanks to coupling between clocks.

Based on a physiological model of peripheral circadian clocks, our theoretical and computational results are among the first to analyze peripheral clock coupling. Our modeling approach provides a dynamical view of the coupling mechanism and illustrates how the coordination between the different stages leads to synchronization of two peripheral oscillators. Our results also show that intercellular coupling of peripheral clocks is a major factor in obtaining a coherent signal in response to feeding schedules.

Acknowledgments

References

[1] S. Almeida, M. Chaves, and F. Delaunay. Control of synchronization ratios in clock/cell cycle coupling by growth factors and glucocorticoids. *Royal Society Open Science*, 7:192054, 2020.

[2] S. Almeida, M. Chaves, and F. Delaunay. Transcription-based circadian mechanism controls the duration of molecular clock states in response to signaling inputs. *J. Theor. Biol.*, 484:110015, 2020.

[3] S. An, R. Harang, K. Meeker, D. Granados-Fuentes, C.A. Tsai, C. Mazuski, J. Kim, F.J. Doyle, L.R. Petzold, and E.D. Herzog. A neuropeptide speeds circadian entrainment by reducing intercellular synchrony. *Proc. Natl. Acad. Sci. USA*, 110(46):E4355–E4361, 2013.

[4] A. Balsalobre, L. Marcacci, and U. Schibler. Multiple signaling pathways elicit circadian gene expression in cultured rat-1 fibroblasts. *Current Biology*, 10(20):1291–1294, 2000.

[5] J. M. Berg, J. L. Tymoczko, and L. Stryer. *Biochemistry (5th ed.)*. W. H. Freeman and Company, New York, 2002.

[6] T. Börding, A.N. Abdo, B. Maier, C. Gabriel, and A. Kramer. Generation of human cry1 and cry2 knockout cells using duplex crispr/cas9 technology. *Frontiers in Physiology*, 10, 2019.

[7] R. Casey, H. de Jong, and J.L. Gouzé. Piecewise-linear models of genetic regulatory networks: equilibria and their stability. *J. Math. Biol.*, 52:27–56, 2006.

[8] A. Korenčič, G. Bordyugov, R. Košir, D. Rozman, M. Goličnik, and H. Herzel. The interplay of cis-regulatory elements rules circadian rhythms in mouse liver. *PLoS ONE*, 7:e46835, 2012.

[9] E. Destici, E.H. Jacobs, F. Tamanini, M. Loos, G.T.J. van der Horst, and M. Oklejewicz. Altered phase-relationship between peripheral oscillators and environmental time in cry1 or cry2 deficient mouse models for early and late chronotypes. *PLOS ONE*, 8(12):1–12, 2013.

[10] D. DeWoskin, J. Myung, M.D.C. Belle, H.D. Piggins, T. Takumi, and D.B. Forger. Distinct roles for gaba across multiple timescales in mammalian circadian timekeeping. *Proc. Natl. Acad. Sci. USA*, 112(29):E3911–E3919, 2015.

[11] C. Feillet, P. Krusche, F. Tamanini, R.C. Janssens, M.J. Downey, P. Martin, M. Teboul, S. Saito, F.A. Lévi, T. Bretschneider, G.T. van der Horst, F. Delaunay, and D.A. Rand. Phase locking and multiple oscillating attractors for the coupled mammalian clock and cell cycle. *Proc. Natl. Acad. Sci. USA*, 111(7):9828–9833, 2014.

[12] A.-M. Finger, S. Jäschke, M. del Olmo, R. Hurwitz, A.E. Granada, H. Herzel, and A. Kramer. Intercellular coupling between peripheral circadian oscillators by tgfβ signaling. *Science Advances*, 7(30):eabg5174, 2021.

[13] A.-M. Finger and A. Kramer. Mammalian circadian systems: Organization and modern life challenges. *Acta Physiologica*, 231:e13548, 2021.

[14] D. Forger and C. Peskin. A detailed predictive model of the mammalian circadian clock. *Proc. Natl. Acad. Sci. USA*, 100(25):14806–14811, 2003.

[15] C.J. Guenthner, M.E. Luitje, L.A. Pyle, P.C. Molyneux, J.K. Yu, A.S. Li, T.L. Leise, and M.E. Harrington. Circadian rhythms of PER2::LUC in individual primary mouse hepatocytes and cultures. *PLoS ONE*, 9(2):e87573, 2014.

[16] J.K. Kim, Z.P. Kilpatrick, M.R. Bennett, and K. Josić. Molecular mechanisms that regulate the coupled period of the mammalian circadian clock. *Biophysical J.*, 106:2071–2081, 2014.

[17] A. Kohsaka, A.D. Laposky, K.M. Ramsey, C. Estrada, C. Joshu, Y. Kobayashi, F.W. Turek, and J. Bass. High-fat diet disrupts behavioral and molecular circadian rhythms in mice. *Cell Metabolism*, 6:414–421, 2007.

[18] A. Mukherji, S. Bailey, B. Staels, and T.F. Baumert. The circadian clock and liver function in health and disease. *J. Hepatology*, 71(1):200–211, 2019.

[19] A. Relógio, P.O. Westermark, T. Wallach, K. Schellenberg, A. Kramer, and H. Herzel. Tuning the mammalian circadian clock: robust synergy of two loops. *PLoS Comput. Biol.*, 7(12):e1002309, 2011.

[20] F. Sinturel, P. Gos, V. Petrenko, C. Hagedorn, F. Kreppel, K.-F. Storch, D. Knutti, A. Liani, C. Weitz, Y. Emmenegger, P. Franken, L. Bonacina, C. Dibner, and U. Schibler. Circadian hepatocyte clocks keep synchrony in the absence of a master pacemaker in the suprachiasmatic nucleus or other extrahepatic clocks. *Genes & Development*, 35(5-6):329–334, 2021.

[21] J.S. Takahashi. Transcriptional architecture of the mammalian circadian clock. *Nature Reviews Genetics*, 18(3):164, 2017.

[22] Z. Travnickova-Bendova, N. Cermakian, S.M. Reppert, and P. Sassone-Corsi. Bimodal regulation of mperiod promoters by creb-dependent signaling and clock/bmal1 activity. *Proc. Natl. Acad. Sci. USA*, 99(11):7728–7733, 2002.

[23] B.D. Weger, C. Gobet, F.P.A. David, F. Atger, E. Martin, N.E. Phillips, A. Charpagne, M. Weger, F. Naef, and F. Gachon. Systematic analysis of differential rhythmic liver gene expression mediated by the circadian clock and feeding rhythms. *Proc. Natl. Acad. Sci. USA*, 118(3):e2015803118, 2021.

[24] A. Woller, H. Duez, B. Staels, and M. Lefranc. A mathematical model of the liver circadian clock linking feeding and fasting cycles to clock function. *Cell Reports*, 17(4):1087–1097, 2016.

[25] A. Woller and D. Gonze. Modeling clock-related metabolic syndrome due to conflicting light and food cues. *Scientific Reports*, 8(1):13641, 2018.

[26] E.E. Zhang, A.C. Liu, T. Hirota, L.J. Miraglia, G. Welch, P.Y. Pongsawakul, X. Liu, A. Atwood, J.W. Huss, J. Janes, A.I. Su, J.B. Hogenesch, and S.A. Kay. A genome-wide rnai screen for modifiers of the circadian clock in human cells. *Cell*, 139(1):199–210, 2009.

Appendix

ε	0.2	0.4	0.6	0.7	0.8	0.85	0.9	0.95
Period (h)	27.2	27.2	26.7	26.3	25.8	25.5	25.2	24.8
ε	1.0	1.05	1.1	1.15	1.2	1.4	1.6	1.8
Period (h)	24.5	24.1	23.8	23.4	23.0	21.4	19.6	17.9

Table 2: Equivalences between ε values and period of (uncoupled) oscillator 2.